

Deuterium retention in re-solidified tungsten and beryllium

J.H. Yu*, M.J. Simmonds, M.J. Baldwin, R.P. Doerner

Center for Energy Research, UC San Diego, 9500 Gilman Dr., La Jolla, CA 92093-0417, USA



ARTICLE INFO

Keywords:

Tokamak plasma-material interactions
Transient heating
Laser melting
Hydrogen retention

ABSTRACT

Leading edges of the ITER tungsten (W) divertor are expected to melt due to transient heat loads from edge localized modes (ELMs), and melting of the entire divertor surface will occur during vertical displacement events (VDEs) and disruptions. In addition, understanding tritium retention in plasma facing materials is critical for the successful operation of ITER due to safety reasons. Thus, the question of how melting affects hydrogenic retention is highly relevant for fusion devices. Here we use an Nd:YAG laser to melt tungsten and beryllium in vacuo, and the samples are subsequently exposed to deuterium plasma with sample temperatures ranging from 370 to 750 K. The deuterium content in re-solidified and reference (no laser) samples is measured using thermal desorption spectroscopy and modeled using TMAP-7. In all cases, the re-solidified samples have lower retention compared to the reference samples. For re-solidified tungsten, the most significant effect is in the 1.8 eV trap with peak thermal desorption temperature of ~750 K, which had a 77% reduction in the peak release rate compared with the reference sample. SEM imaging indicates that laser melting and re-solidification of tungsten anneals intrinsic defects that act as nucleation sites for larger-scale defects that develop during plasma exposure. However, melting does not significantly affect traps with lower de-trapping energies of 1.0 eV and 1.4 eV. In beryllium, melting and cracking results in lower retention compared to the reference sample by 40%, and thermal desorption profiles indicate that the diffusion depth of deuterium into re-solidified beryllium is lower than that of the reference sample.

1. Introduction

Tungsten (W) is a candidate plasma facing material (PFM) for future fusion reactors due to its low sputtering rate and high melting point [1], and beryllium (Be) will be used for the first wall due to its low plasma contamination as a low-Z material and its capability as an oxygen getter [2]. Extrapolation from current tokamaks to ITER predicts that edge localized modes (ELMs), VDEs, and disruptions will melt parts of the W divertor, particularly leading edges [3]. Significant heating of the Be first wall can also occur, as demonstrated by accidental melting of beryllium in the JET tokamak with the ITER-like wall [4]. In addition, understanding and preventing excessive tritium retention in PFM is crucial for safety reasons and for the development of an effective fuel cycle [5]. Thus, the question of how melting affects hydrogenic retention in W and Be is highly relevant for fusion devices, but limited data is available. Does melting/re-solidification create additional trap sites and thus increase retention, or, does melting anneal intrinsic defects and decrease retention?

Previous work [6] on re-solidified tungsten claimed that deuterium (D) retention on the surface of a melted layer was not significantly different from the non-melted sample, and that retention was increased

in the bulk of the re-solidified sample; however, the surface was contaminated with carbon and the signal-to-noise of the nuclear reaction analysis (NRA) measurement was low. In JET, a ten-fold reduction of D surface concentration was observed due to simultaneous melting from ELMs on a modified sloped W lamella [7]. In other work using simultaneous laser heating with plasma on W in the PSI-2 facility, a 12x increase in retention was observed [8]. These seemingly conflicting results indicate additional work is necessary to accurately predict the retention behavior in future tokamaks. To the best of our knowledge, no work has been done previously on hydrogenic retention in re-solidified beryllium.

The procedure used here can be considered melt annealing on a millisecond timescale, and our experiments provide insight into how material will perform following a large thermal transient event in ITER. In addition, lasers have been proposed as a method to diagnose and desorb tritium [9–15] from plasma-facing components in future fusion devices, as well as a melting tool to “repair” tungsten that may become cracked after being subjected to a large number of mitigated ELM heat loads [16]. The question we address in the present work is how laser melting affects hydrogenic uptake during subsequent plasma exposure.

* Corresponding author.

E-mail address: j2yu@eng.ucsd.edu (J.H. Yu).

2. Materials and methods

We compare deuterium retention in re-solidified tungsten and beryllium with retention in non-melted reference samples. Samples are first melted using laser heating and then exposed to D plasma, following by thermal desorption spectroscopy (TDS). A confocal laser microscope and scanning electron microscope (SEM) are used to image the samples before and after plasma exposure.

Tungsten samples from Midwest Tungsten were cut from 99.95 wt% powder metallurgy polycrystalline W rod, 6 mm in diameter and 1.5 mm thick. The grains were orientated perpendicular to the sample surface. The front surfaces of the samples were mechanically polished producing a mirror finish with arithmetic mean surface roughness of approximately 50 nm. The samples were then cleaned in separate acetone and ethanol ultrasonic baths. To achieve the same amount of intrinsic defects and relieve stress, all samples were initially annealed by heating the samples at 0.5 K/s to 1173 K and holding for 1 h at pressure below 10^{-4} Pa. Be samples were 10 mm in diameter and unpolished. A subset of the samples consisting of W or Be was then melted using an Nd:YAG laser with wavelength 1064 nm in a vacuum chamber with pressure below 5×10^{-5} Pa (no concurrent plasma). The laser spot size ($1/e^2$ spot diameter of ~ 0.5 mm) was smaller than the sample diameter and therefore the laser was rastered across the sample in order to cover the entire sample surface, with each spot overlapping the previous spot's area by approximately 20–40%. The laser was fired once in each spot with a waiting time between shots of at least two seconds. Two laser conditions were used on tungsten with heat flux factors of $150 \text{ MJm}^{-2}\text{s}^{-1/2}$ and $110 \text{ MJm}^{-2}\text{s}^{-1/2}$, both with 10 ms pulse width. Tungsten samples were melted with approximately 100 laser spots. Beryllium was irradiated with 350 laser shots, each with heat flux factor of $62 \text{ MJm}^{-2}\text{s}^{-1/2}$ and pulse width 1 ms. The temporal shape for all pulses was approximately rectangular. The absorbed laser power densities quoted in the present work were calculated based on measurements of the laser pulse width, laser energy measured outside the vacuum chamber, laser melt area obtained from confocal microscopy of the laser-irradiated samples, and assuming a constant reflectivity of 0.6 and 0.4 for tungsten [17] and beryllium [18], respectively. Changes to the reflectivity during and following laser heating [19] were not taken into account here.

Thermal emission from the sample surfaces was measured with a

multi-color pyrometer [20], and the inferred temperature is shown in Figs. 1b and 2b along with the absorbed power densities in Figs. 1a and 2a. On tungsten, the pyrometer recorded a peak surface temperature of 4620 K for the $150 \text{ MJm}^{-2}\text{s}^{-1/2}$ pulse and 3490 K for the $110 \text{ MJm}^{-2}\text{s}^{-1/2}$ pulse, and on beryllium, 2260 K for the $62 \text{ MJm}^{-2}\text{s}^{-1/2}$ 1 ms pulse. The pyrometer viewing spot size was larger than the laser spot size and therefore the resulting temperature was an emission-weighted average. For this reason, the typical flattening of the temperature evolution at the melting/re-solidification temperature was not readily apparent. Following laser-induced melting, samples were exposed to deuterium plasma with ion energy of 70–100 eV. Re-solidified and reference tungsten samples were exposed simultaneously to the same deuterium plasma in the PICSES-A linear plasma device. The sample temperature was monitored with a thermocouple on the back-side of the air-cooled samples, and the experiment was repeated using three different plasma exposures with different sample temperatures. The PICSES-A plasmas ranged in electron density from $0.5 \times 10^{18} \text{ m}^{-3}$ to $1.1 \times 10^{18} \text{ m}^{-3}$ and in T_e from 2.0 to 4.5 eV. For the beryllium samples, the re-solidified and the reference samples were exposed to separate deuterium plasmas in the PICSES-B plasma device [21] using nearly identical plasma conditions with ion flux of $1.7 \times 10^{22} \text{ Dm}^{-2}\text{s}^{-1}$ for 588 s, electron density $n_e = 1.6\text{--}1.8 \times 10^{18} \text{ m}^{-3}$, and electron temperature $T_e = 4.6$ to 6.5 eV. In both PICSES-A and PICSES-B, the plasma parameters were measured with a Langmuir probe inserted approximately 25 mm in front of the sample location, and the radial profiles of n_e and T_e were measured to be uniform across the samples to within $\sim 15\%$. Re-solidified W samples were transferred in air to PICSES-A after laser melting for subsequent plasma exposure, while the Be sample was melted and then exposed to plasma with no air exposure. The term “pre-melted” is used throughout this paper to refer to the fact that laser melting was performed before plasma exposure.

Following plasma exposure, the samples were thermally desorbed to measure the amount of trapped deuterium and infer trap release energies using TMAP-7 modeling. During TDS, tungsten samples were heated from 300 to 1270 K at 0.5 K/s and the released D_2 , HD , and H_2 were monitored by a residual gas analyzer which was calibrated with a known D_2 leak rate. A literature review by Causey supports the notion that most, if not all, hydrogenic species are removed from tungsten at a TDS temperature of 1270 K [22]. The maximum TDS temperature for beryllium was limited to 920 K to avoid coating the TDS chamber. A

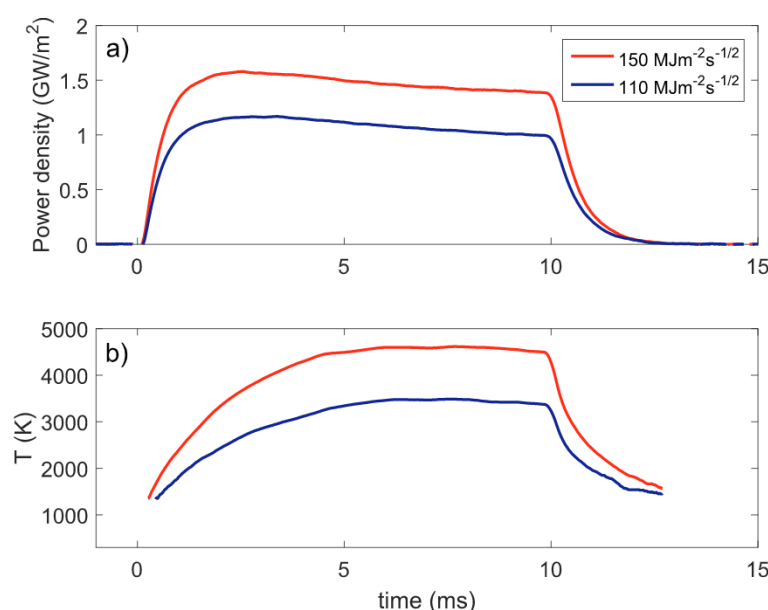


Fig. 1. (a) Absorbed laser power density on tungsten for two heat flux factors. (b) The measured surface temperature.

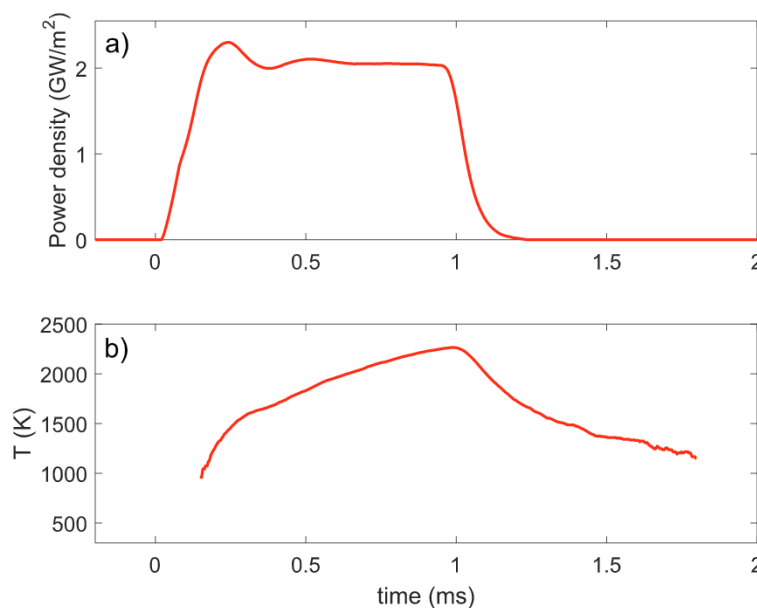


Fig. 2. (a) Absorbed laser power density on beryllium. (b) The measured surface temperature.

background subtraction method [15] was used to eliminate the spurious H₂ contribution to the HD and D₂ signals, and the sensitivity for HD was assumed to be the same as that for D₂.

3. Results

3.1. TMAP-7 modeling

The reaction diffusion code TMAP-7 [23] was used to model plasma implantation and TDS of tungsten self-consistently using the measured D flux and sample temperatures throughout the plasma exposure. Modeling parameters were optimized to fit the experimental TDS curve. Modeling of beryllium was not performed due to an unreasonably large parameter space arising from uncertainties in the trap profiles, concentrations, and surface effects. For tungsten, Anderls recombination coefficient and the mass corrected Fraunfelder diffusion constant were used [24], and an attempt frequency of 10¹³ s⁻¹. The ratio of implanted ion flux to the incident ion flux was taken to be 9 × 10⁻⁵, which is consistent with that required to match results in other relatively high ion flux experiments [25]. However, this low implantation fraction implies an effective ion reflection coefficient that is much larger than that predicted by Eckstein [26], and this discrepancy is currently an unresolved issue within the hydrogen-tungsten modeling community.

Traps were modeled as intrinsic traps represented by a spatially uniform trap concentration throughout the sample, or as having a near-surface exponential decay of trap concentration in addition to an offset representing intrinsic defects. The exponential decay of trap concentration is motivated by previous NRA measurements of D spatial profiles in tungsten [27,28] which typically reveal a D peak in the near surface implantation zone. This peak suggests defects are created and populated by D implantation, possibly due to deuterium super-saturation in the plasma implantation zone that stresses the tungsten lattice [29–31]. The modeled TMAP-7 trap concentration has the form

$$c = a + b \exp\left(-\frac{x}{x_0}\right),$$

where a is the intrinsic trap concentration, b is the scale factor for the near-surface profile of trap concentration, x is the depth coordinate, and an e-folding length of $x_0 = 60$ nm is used. However, without D depth profile measurements the modeling results should be interpreted with

caution.

During the fit to experimental TDS spectra, TMAP-7 model parameters were allowed to vary $+/- 10\%$ from initial parameter values, which were manually determined from previous experience. Final parameters were determined by minimizing the normalized root mean square error (NRMSE) between the TMAP-7 TDS spectrum and the measured TDS spectrum. Up to three traps were modeled and each parameter (when used) was varied one at a time in the following order: $E1$ through $E3$, $a1$ through $a3$, then $b1$ through $b3$. The process was repeated until NRMSE was below 20%. Manual adjustments to parameters were made when necessary and the fitting procedure was restarted, which meant that in practice the parameters were varied by more than $+/- 10\%$, particularly parameters a and b .

3.2. Re-solidified tungsten

3.2.1. TDS

Fig. 3 shows TDS curves from three sets of deuterium plasma exposures spanning a range of sample temperatures from 370 K to 750 K. Results of TMAP-7 modeling are shown as dashed lines, and model parameters of intrinsic and near-surface trap concentrations, as well as de-trapping energies, are listed in Table 1.

In Fig. 3a, the pre-melted and reference samples were exposed to D plasma with initial ion flux and sample temperature of $7.2 \times 10^{21} \text{ Dm}^{-2}\text{s}^{-1}$ and 590 K, respectively. These parameters were decreased to $3.7 \times 10^{21} \text{ Dm}^{-2}\text{s}^{-1}$ and 420 K by 900 s, further decreased to $2.0 \times 10^{21} \text{ Dm}^{-2}\text{s}^{-1}$ and 370 K by 3060 s, and then held constant until the end of the exposure at 7380 s. The sample was biased to achieve incident ion energy of 70 eV. The initial elevated temperature mobilized D which allowed filling of traps deeper within the material, and may have also enabled the development of vacancy clusters and voids. The lower temperature during the remainder of the exposure enabled traps with lower de-trapping energy to be populated. The result is that the reference sample had two prominent TDS release peaks located near 450 K and 750 K with de-trapping energies modeled as 1.0 eV and 1.8 eV, respectively. A third trap with de-trapping energy of 1.3–1.5 eV was also used in the modeling. The pre-melted samples had a lower retention in the 1.8 eV because laser heating annealed intrinsic defects during melting and recrystallization. Pre-treatment with $110 \text{ MJm}^{-2}\text{s}^{-1/2}$ and $150 \text{ MJm}^{-2}\text{s}^{-1/2}$ laser pulses caused the peak desorption flux from this trap to decrease by 65% and 77%,

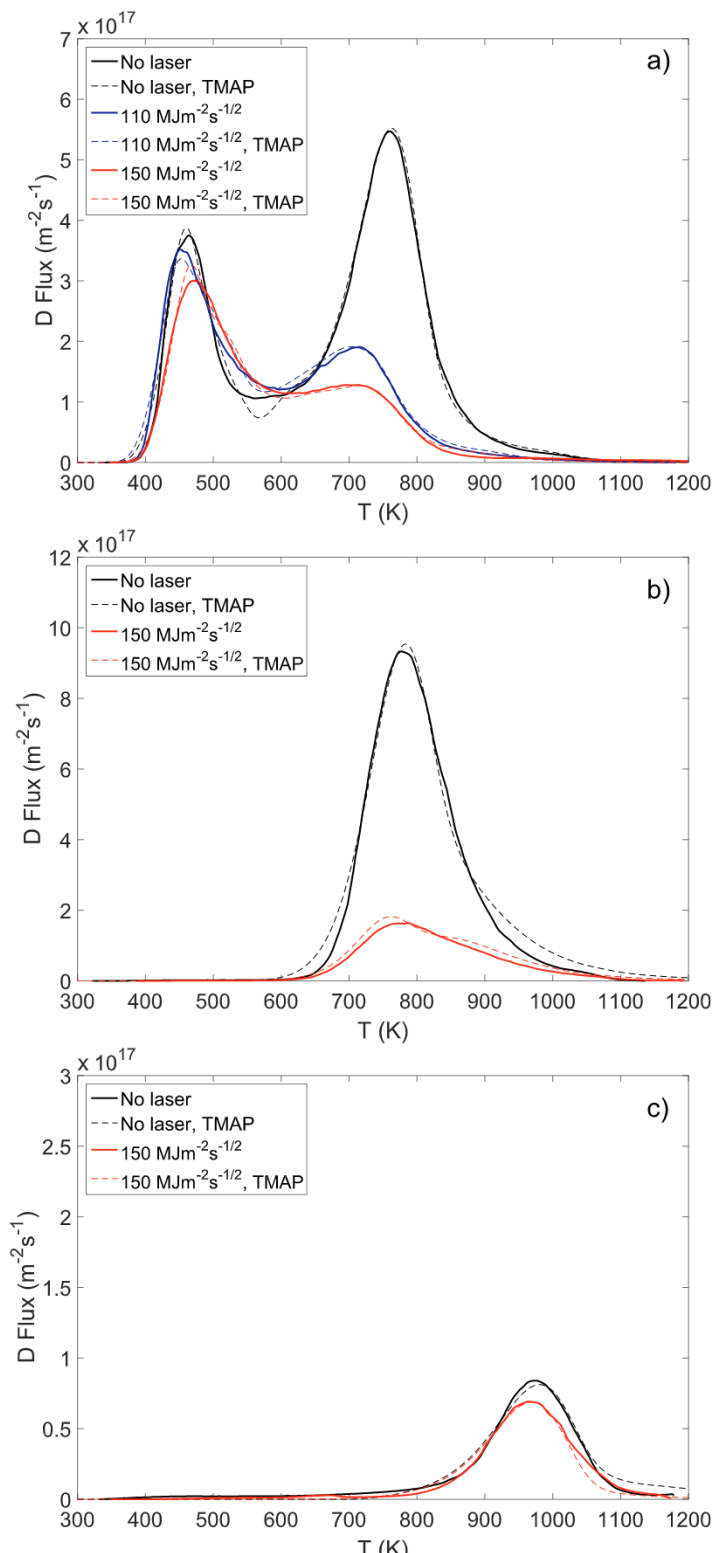


Fig. 3. TDS curves (solid lines) and TMAP-7 modeling (dashed). Reference samples shown as black and re-solidified samples shown as red and blue. (a) Sample temperatures during plasma exposure initially at 590 K and then held at 370 K. (b) Sample temperatures of 600 K during D plasma. (c) 750 K sample temperatures during D plasma. (For interpretation of the references to colour in this figure legend, the reader is referred to the web version of this article.)

respectively. Interestingly, the 1.0 eV and 1.4 eV traps were not significantly affected by pre-melting, which suggests that these traps were induced during plasma exposure as both the reference and pre-melted sample were exposed to the same plasma.

In higher sample temperature of 600 K during plasma exposure,

with plasma flux $2.0 \times 10^{21} Dm^{-2}s^{-1}$ for 5100 s and 70 eV ion energy, pre-melting caused a 76% reduction of the D_2 peak release rate from the 1.8 eV trap as shown in Fig. 3b. The 1.0 and 1.4 eV traps were absent in the TDS curves because thermo-desorption during plasma exposure prevented these traps from remaining populated. A single de-trapping

Table 1

Tungsten TMAP-7 model parameters, a and b , used for trap concentrations and de-trapping energy, E . Laser heat flux factor (HFF) listed in units of $\text{MJm}^{-2}\text{s}^{-1/2}$, fluence in units of (10^{25} m^{-2}) and retention in units of $(10^{20} \text{ Dm}^{-2})$. a and b are in units of atomic fraction.

Laser HFF	T_{exp} (K)	Fluence	Retention	E_1 (eV)	a_1	b_1	E_2 (eV)	a_2	b_2	E_3 (eV)	a_3	b_3
0	370–590	1.92	2.38	1.01	2.8×10^{-5}	7.9×10^{-3}	1.46	1.8×10^{-5}	2.1×10^{-3}	1.80	1.5×10^{-7}	2.1×10^{-2}
110	370–590	1.92	1.52	0.99	3.6×10^{-5}	5.0×10^{-3}	1.33	2.3×10^{-5}	6.1×10^{-4}	1.78	5.8×10^{-8}	2.4×10^{-3}
150	370–590	1.92	1.28	1.03	2.1×10^{-5}	6.4×10^{-3}	1.34	8.6×10^{-6}	6.1×10^{-4}	1.81	4.7×10^{-8}	1.6×10^{-3}
0	600	1.01	2.77	N/A	N/A	N/A	N/A	N/A	N/A	1.81	4.6×10^{-4}	4.6×10^{-2}
150	600	1.01	6.75	N/A	N/A	N/A	N/A	N/A	N/A	1.81	7.3×10^{-5}	4.9×10^{-3}
0	750	3.90	0.28	N/A	N/A	N/A	2.06	2.5×10^{-6}	N/A	2.42	5.0×10^{-7}	1.4×10^{-3}
150	750	3.90	0.23	N/A	N/A	N/A	2.06	2.5×10^{-6}	N/A	2.40	5.0×10^{-7}	1.4×10^{-3}

energy was used to model ion implantation and thermal release during TDS. The spatial profile of the modeled 1.8 eV trap concentration required a near-surface distribution in order to match the relatively narrow desorption peak observed in the TDS spectra.

At even higher sample temperature of 750 K during an 8640 s plasma exposure with flux of $4.5 \times 10^{21} \text{ Dm}^{-2}\text{s}^{-1}$ and 100 eV ion energy, the total retention for the reference and pre-melted samples decreased to $2.5 \times 10^{19} \text{ Dm}^{-2}$ and $2.3 \times 10^{19} \text{ Dm}^{-2}$, respectively, as shown in Fig. 3c. The de-trapping energies required to model the data shifted to higher energies of 2.1 and 2.4 eV, with an exponential decay of trap concentration used in the 2.4 eV trap. The shift in de-trapping energy was most likely due to the growth of vacancy clusters from mobility and agglomeration of mono-vacancies at elevated temperature. This mechanism has been studied previously in [32], which found that the growth of clusters begins at approximately 600 K and the de-trapping energy from clusters was 2.1 eV.

The tungsten retention results are summarized in Fig. 4. The largest retention was measured in a reference sample exposed at approximately 500 K for 12,780 s with a fluence of $3.9 \times 10^{25} \text{ Dm}^{-2}$. The largest effect due to pre-melting is seen in the 600 K exposure due to the reduction of the 1.8 eV trap population.

3.2.2. Tungsten images

Surface images of reference and laser-irradiated tungsten samples are shown in the left and right side columns of Fig. 5, respectively. The top row (Fig. 5a and b) shows confocal microscope images, and the other images were obtained with an SEM after plasma exposure. Overlapped laser melt craters and recrystallized grains are visible in Fig. 5b. The high magnification images in the lower three rows of Fig. 5c–h were obtained after the three plasma exposures previously discussed for Fig. 3, with Fig. 5c–d corresponding to sample

temperatures of 370–590 K during plasma exposure (TDS curves in Fig. 3a), Figs. 5e–f showing samples exposed at 600 K (Fig. 3b), and Fig. 5g–h showing samples exposed at 750 K (Fig. 3c). Samples with the largest differences in D retention due to pre-melting displayed the most striking differences in surface morphology. This can be seen by comparing the left and right side columns of Fig. 5c–f, which reveal that the reference samples have significantly more surface features compared to the re-solidified surfaces. During plasma exposure at 600 K and below, the reference samples developed pits and features similar to ruptured blisters, while the pre-melted samples, which were exposed to the same plasma as the reference samples, did not.

The 150 $\text{MJm}^{-2}\text{s}^{-1/2}$ pre-melted sample exposed at low temperature shown in Fig. 5d had a smooth re-solidified surface; a grain boundary running diagonally across the image is also visible. The 110 $\text{MJm}^{-2}\text{s}^{-1/2}$ pre-melted sample (not shown) had a similarly smooth surface after plasma exposure. In Fig. 5f, the pre-melted sample exposed at 600 K retained a relatively smooth surface but also developed fine-scale ripples during plasma exposure. At sample temperature of 750 K, both the reference and the re-solidified tungsten surfaces developed a terraced surface morphology on certain grains as seen in Fig. 5g and h, and both of these samples had low but similar D retention. The development of terraces depended on crystal orientation as only some grains displayed this type of morphology.

Further insight into the effect of laser heating on tungsten can be seen in cross section SEM images, which are shown in Fig. 6 for plasma-exposed samples at 600 K. The laser affected zone is approximately 100 μm deep and consists of a melt layer extending to $\sim 50 \mu\text{m}$, and recrystallized grains that extend an additional $\sim 50 \mu\text{m}$, as seen in Fig. 6b. Modeling reveals that traps were filled with deuterium in this sample to a depth of 15 μm , and in longer plasma exposures to a depth of 50 μm . The re-solidified region is seen as columnar grains oriented

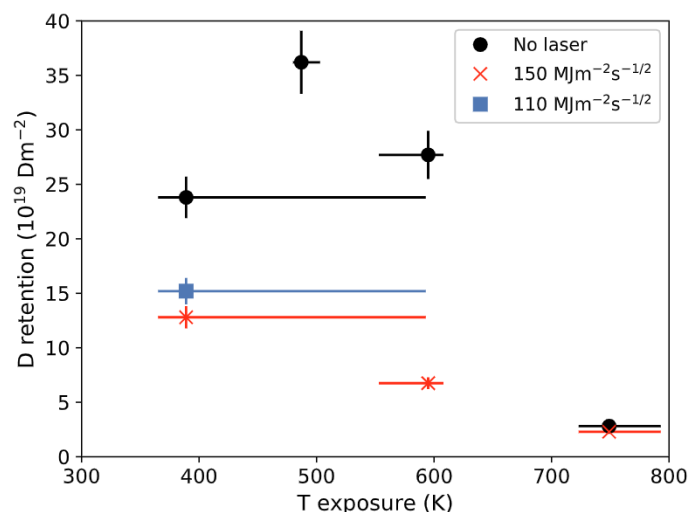


Fig. 4. D retention in tungsten for reference samples (circles), and re-solidified samples for two laser conditions (x's and squares). The horizontal bars represent the range of sample temperatures during exposure; horizontal locations of the data points show the time-weighted average temperature during plasma exposure.

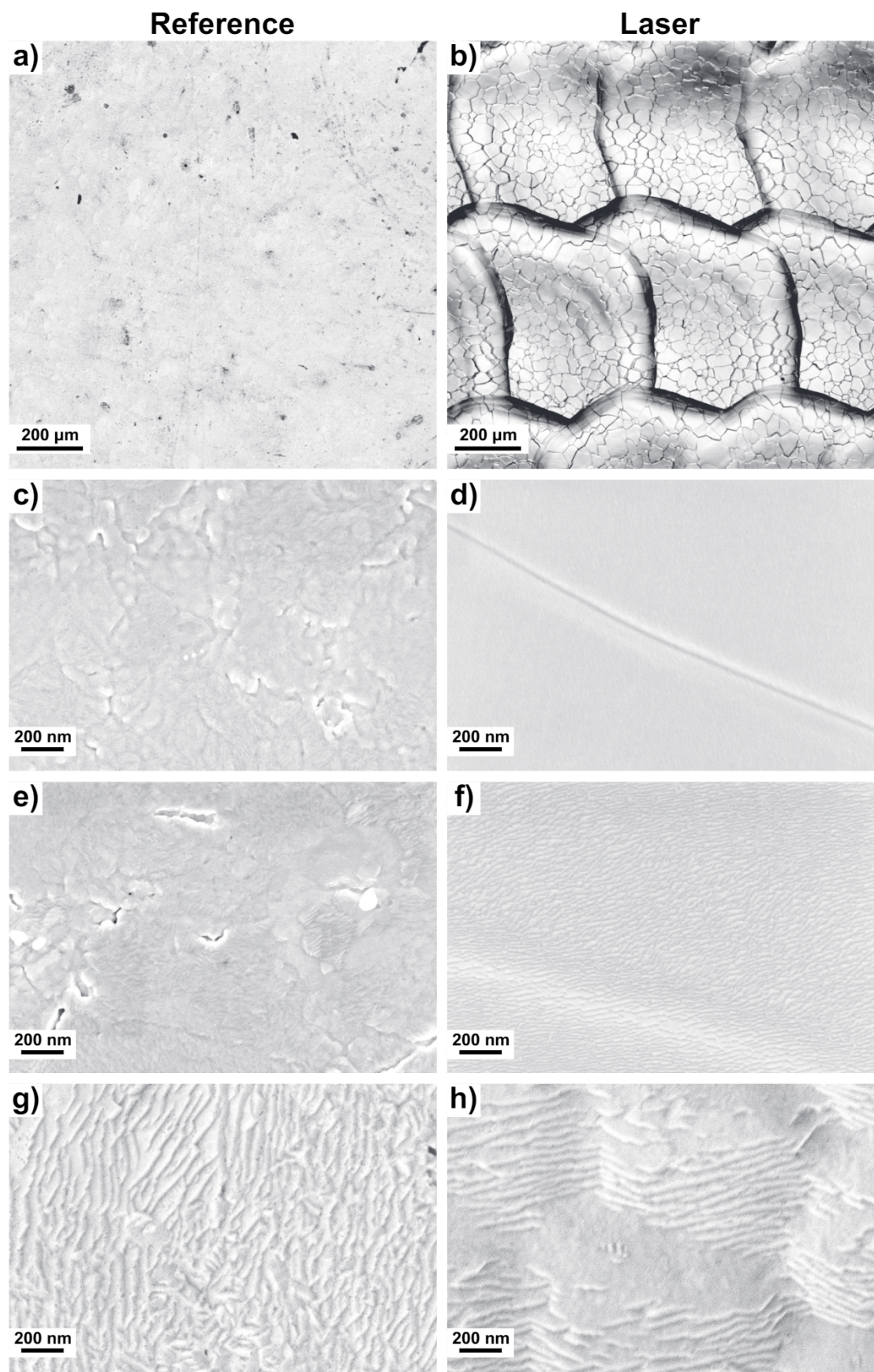


Fig. 5. Tungsten surfaces of reference samples (left column) and re-solidified samples (right column) following plasma exposure. Top row: confocal microscope images of (a) polished sample and (b) rastered laser melt craters. (c)–(d) SEM images of 590–370 K samples, (e)–(f) 600 K samples, (g)–(h) 750 K samples.

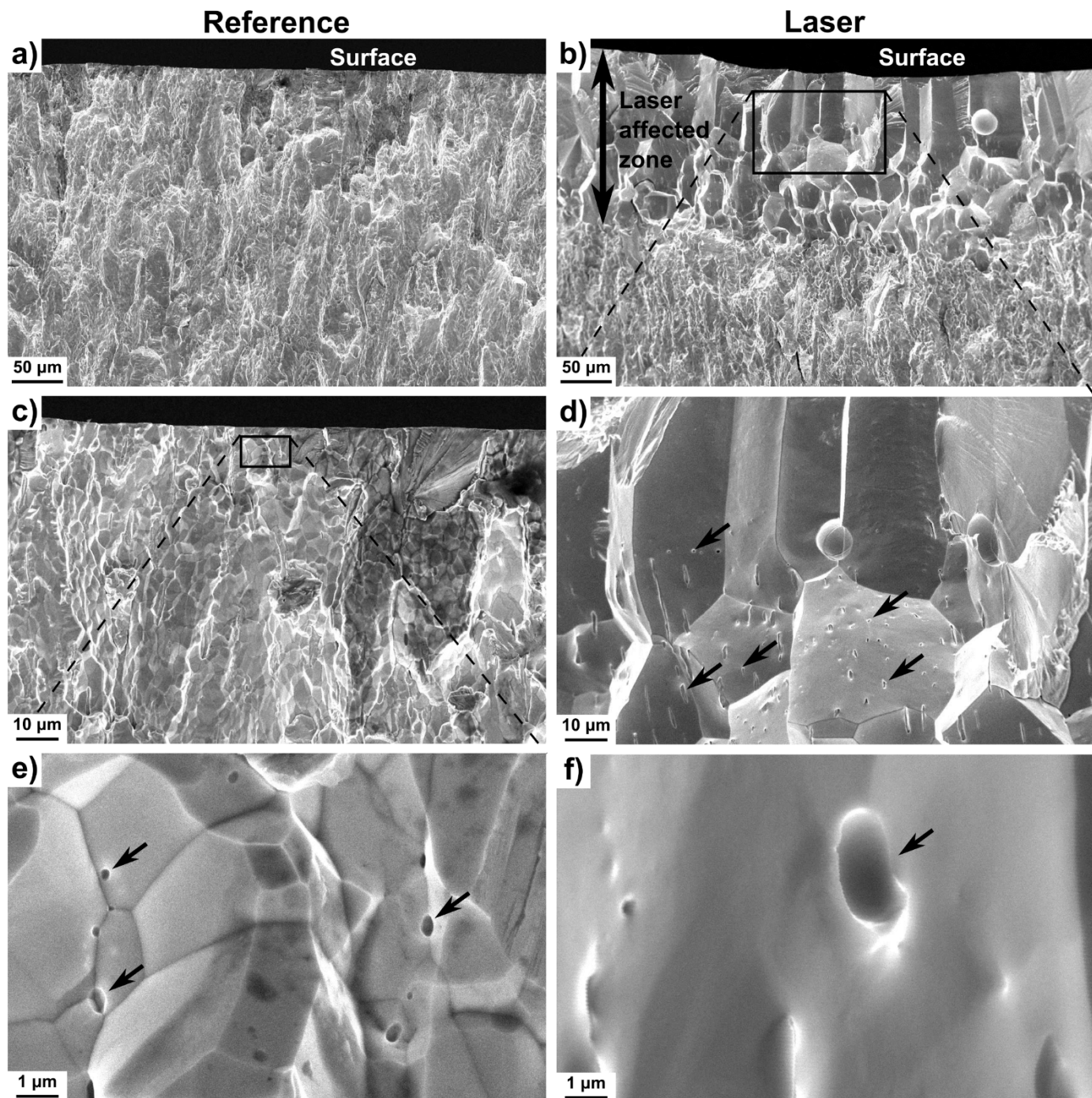


Fig. 6. Cross-section SEM images of tungsten reference (left column) and re-solidified (right column) samples from 600 K plasma exposure. Laser direction is from top of images toward bottom. (a) Polycrystalline tungsten with grains oriented perpendicular to surface. (b) Laser melting to a depth of ~50 μm. (c)–(d) Pores are marked with black arrows in recrystallized tungsten, no pores visible in melt layer. (e)–(f) Larger pore size in recrystallized material.

perpendicular to the surface. Lower aspect ratio recrystallized grains are located deeper within the sample. Confocal microscopy revealed that each laser pulse deformed the surface into a crater approximately 20–30 μm deep due to the motion of molten tungsten, which was presumably driven by laser-induced recoil pressure and thermo-capillary forces [33].

Sub-micron sized cavities, or pores, are visible in the SEM images. These pores were created during material processing and are located throughout the reference sample. A select number of pores are marked with arrows in Fig. 6e. However, in the pre-melted samples, no pores were visible in the ~50 μm melt layer. Pores become visible

approximately 50 μm below the surface as seen in Fig. 6d, and the pores are elongated in the direction of the temperature gradient induced by the laser. In the pre-melted samples, pores are larger than those observed in the reference sample, with linear dimensions of 1–2 μm and 100–200 nm, respectively. Pores may act as trapping sites for D₂ [34] and the melt-annealing of near-surface pores in the pre-melted samples could partially explain their lower D retention. It is reasonable to assume that, based on the elimination of pores in the re-solidified layer, smaller scale intrinsic defects are also annealed. However, it is important to note that the physics of deuterium forming the gas phase inside a pore, and the requirement to go back into solution in order to

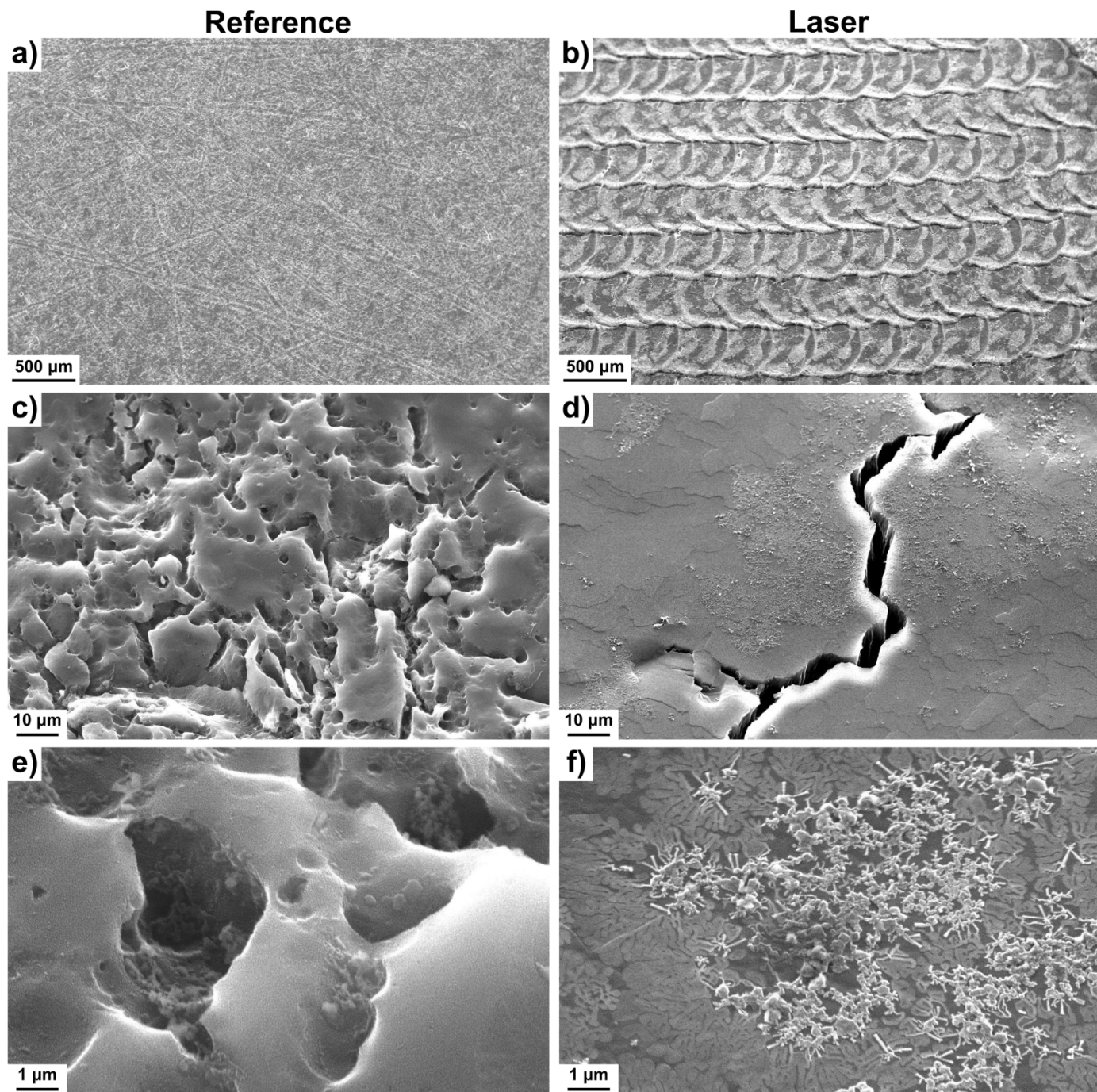


Fig. 7. Top surfaces of beryllium reference (left column) and re-solidified/cracked samples (right column) after plasma exposure and before TDS.

reach the sample surface to be released, is not included in TMAP-7 simulations.

3.3. Re-solidified beryllium

Be was melted using rastered laser pulses with approximately 2 GW/m^2 of absorbed power density in each 1 ms pulse (see Fig. 2). The pre-melted Be was then exposed to deuterium plasma and with sample temperature of 410 K for a total fluence of $1.0 \times 10^{25} \text{ Dm}^{-2}$. SEM images of the Be reference and laser-irradiated samples are shown in the left and right columns of Fig. 7, respectively. Significant morphology is visible in the unpolished reference sample in Fig. 7c and d. Rastered laser spots are shown in Fig. 7b, and cracks developed within all laser spots as shown in Fig. 7d. Interestingly, crystal dendrites were

created when molten Be rapidly solidified immediately following the laser pulse, as shown in Fig. 7f. These types of crystal patterns were also observed in areas of re-solidified Be following laser melting of $2 \mu\text{m}$ beryllium layers on tungsten [35] (although dendrite images were not shown in the previous work). The dendrites were only visible in parts of each laser spot most likely where the cooling front evolution and a lack of surface nucleation sites created energetically favorable conditions for supercooling. Crystal dendrites were sputtered by deuterium ions, as evidenced by the lack of dendrites following plasma exposure.

The pre-melted Be sample had a lower deuterium retention compared to the reference sample by 40% with retention of $2.23 \times 10^{20} \text{ Dm}^{-2}$ and $3.73 \times 10^{20} \text{ Dm}^{-2}$, respectively. The TDS curves in Fig. 8 exhibit sharp thermal release peaks between 525 and 550 K, following by lower release flux at higher temperatures. The

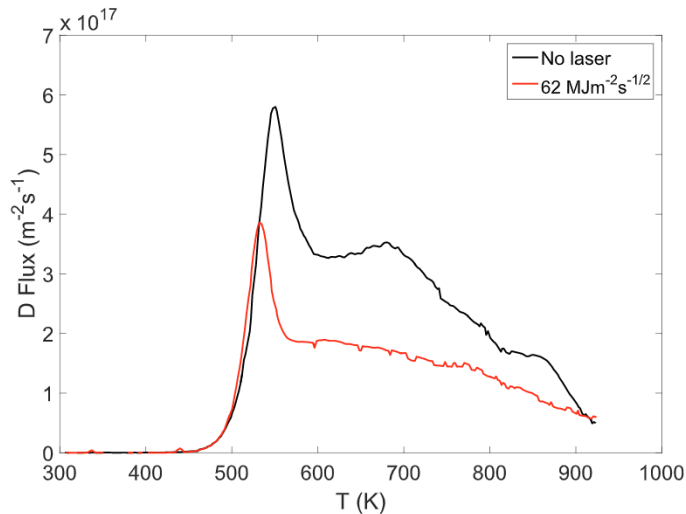


Fig. 8. TDS of beryllium reference and re-solidified/cracked samples.

reference sample has at least one higher energy trap as indicated by the release peak near 675 K, and possibly another release peak near 850 K. The relative shapes of the TDS curves indicate that Be was confined in a thinner layer in the re-solidified sample compared to the reference sample. This can be seen from previous work by Baldwin in which controlled Be-D layers were created with varying thicknesses ranging from 0.2 to 0.7 μm , and thermal desorption during TDS was modeled using TMAP-7. The TDS curves in Fig. 1 of [36] show similar behavior as the Be samples here, namely that the TDS release for the thinner Be layer follows the thicker layer until a certain desorption temperature, then suddenly decreases. The result is that the thinner layer has a peak thermal desorption flux that is smaller and shifted to lower temperature compared to the thicker layer. In [36], it was also demonstrated that the peak release temperature was linearly proportional to the layer thickness. This behavior is in contrast to TDS curves for tungsten in Fig. 3, in which the peak release temperatures are roughly the same for the pre-melted and reference samples, but the lower concentration of trapped D caused a decrease in the peak height.

4. Discussion

The low temperature W release peak with de-trapping energy of 1.0 eV is typically associated with dislocations and mono-vacancies, and is also at the upper end of energies associated with trapping at grain boundaries [37]. In our re-solidified samples, the grain structure was drastically altered due to melting and recrystallization with columnar grains in the near surface region extending to a depth of $\sim 50 \mu\text{m}$ (compare the reference and pre-melted samples in Fig. 6). The lack of significant change to the 1.0 eV trap in pre-melted tungsten suggests that in our samples this release peak is not due to grain boundaries, and therefore we associate this peak in our samples with dislocations and mono-vacancies.

Tungsten de-trapping energies from 1.8 to 2.4 eV have been attributed to hydrogenic trapping in vacancy clusters [37–38]. Our reference sample data indicate that the 1.8 eV peak grows with plasma exposure temperature up to $\sim 500 \text{ K}$, and then decreases. This behavior suggests that vacancy clusters develop during plasma exposure, and is qualitatively similar to the retention behavior reported in [29], which showed a peak retention at exposure temperature of approximately 500 K with a plasma flux of $1.0 \times 10^{22} \text{ Dm}^{-2}\text{s}^{-1}$. The mechanism responsible for increasing retention in this trap is most likely dependent on both exposure temperature and flux. A significant result from our work is that in re-solidified tungsten the growth of vacancy clusters is suppressed.

A striking difference between surface morphologies of the reference

and pre-melted W is seen on the samples with the largest differences in D retention (Fig. 5c–f). The reference samples with a large 1.8 eV release peak show surface modifications which resemble ruptured blisters, while the re-solidified samples had relatively smooth surfaces. Our data indicate that pre-melting tungsten using disruption-like heat pulses of the order $150 \text{ MJm}^{-2}\text{s}^{-1/2}$ suppresses deuterium retention by annealing intrinsic defects that act as seeds for vacancy cluster growth during plasma exposure. However, pre-melting does not significantly affect traps with lower de-trapping energies of 1.0 and 1.4 eV.

It is useful to compare our results to previous work on the effect of annealing and microstructural changes on deuterium retention in tungsten. In [28], tungsten was recrystallized for 20–60 min before exposing to deuterium plasma, and a decrease of D retention by approximately a factor of 2 was measured in the sample with 2000 K recrystallization temperature. Strong blistering was observed on the reference sample in [28], while no blisters developed in the recrystallized samples. Recrystallization shifted and consolidated the TDS release peaks in [28], and these types of changes were not observed in our data possibly due to the faster timescale of laser annealing. However, the similar reduction of D retention in recrystallized [28] and in the re-solidified tungsten presented here suggests a similar mechanism may be at play.

In beryllium, it is known that deuterium retention saturates with fluence [39] which indicates there is a limit to the diffusion of D. In re-solidified Be, the effective diffusion depth is even smaller than that in non-melted beryllium. One possibility is that laser melting and cracking limits diffusion of D into the material because the presence of cracks allows D that enters the sample to escape before being trapped.

Using sequential rather than simultaneous heating and plasma exposure allows studying the effect of melting/re-crystallization in isolation, without synergistic effects from plasma exposure. However, in a tokamak environment the heat flux will occur simultaneously with plasma flux. The solubility of hydrogenic species in molten material may be significantly higher than that in solid material, and therefore further work is required to predict the retention behavior of material melted due to transient heat loads in ITER. Multiple effects might occur during simultaneous transient heating and plasma loading, including annealing of defects, outgassing from elevated temperature, enhanced hydrogen clustering due to mobility along shock-induced cracks, and increased diffusion of D into W due to large temperature gradients during thermal transients.

Furthermore, sequential exposure to laser heating in the PSL-2 facility with power density of 0.38 GW/m^2 (1 ms pulse width) followed by deuterium plasma resulted in increased retention by more than a factor of 3.6 compared to plasma loading only [8]. Our results show the

opposite effect, namely a decrease in retention with sequential laser and plasma treatment. The heat flux factors in our experiments were approximately an order of magnitude larger than those used in [8], and the difference in retention behavior is most likely explained by the fact that tungsten was melted in our experiments while the heat loads used by Huber et al. caused surface roughening and cracking, but no melting. Enhanced blistering was observed in [8], whereas in our case melting suppressed the formation of surface features that develop during plasma exposure. In addition, the purity of tungsten has a strong effect on whether laser heating forms bubbles in the sub-surface layer, and these bubbles may act as trap sites. In [8], 99.5 wt% was used while in the present work the tungsten purity was 99.95 wt%.

5. Conclusions

In our experiments using sequential melting and plasma exposure, the reduction of D retention in pre-melted tungsten samples is most pronounced in the 1.8 eV trap with TDS release peak near 750–800 K, with lower retention in the re-solidified sample by 77% compared to the reference sample. SEM imaging revealed surface morphology resembling ruptured blisters developed during plasma exposure, however, these surface features were absent on the re-solidified samples following plasma exposure. Thus, laser melting of tungsten anneals intrinsic defects that act as nucleation sites for the development of surface morphology and deuterium trapping sites. A lower D retention is also measured in re-solidified beryllium, but the mechanism is different than that in tungsten; in re-solidified beryllium, an effective D diffusion barrier is created which results in a shallower D layer compared to the reference sample. This work shows that while melting is generally unwanted, and certainly cracking would be deleterious in ITER, melting may provide the potential benefit of reducing hydrogenic uptake during subsequent plasma exposure.

Future work includes measuring depth profiles of deuterium within laser spots, as this would provide constraints on model parameters. In addition, displacement damage due to neutrons will create additional traps for hydrogenic species, and therefore potential tritium control measures should be investigated including laser melting as a possible way to anneal displacement damage.

Acknowledgment

This work was supported by USDOE grant DE-FG02-07ER54912.

References

- [1] G. Federici, Nucl. Fusion 41 (2001) 1967.
- [2] R.W. Conn, Fusion Eng. Des. 37 (1997) 481.
- [3] R.A. Pitts, Nucl. Mat. Energy 12 (2017) 60.
- [4] G. Sergienko, Phys. Scr. T159 (2014) 014041.
- [5] G.R. Tynan, Nucl. Mater. Energy 12 (2017) 164.
- [6] Y. Hamaji, et al., Nucl. Mat. Energy 12 (2017) 1303.
- [7] J.W. Coenen, et al., Phys Scr. T170 (2017) 014013.
- [8] A. Huber, Nucl. Mater. Energy 9 (2016) 157.
- [9] A. Huber, Phys. Scr. T94 (2001) 102.
- [10] C.H. Skinner, N. Bekris, J.P. Coad, C.A. Gentilea, M. Glugla, J. Nucl. Mater. 313 (2003) 496.
- [11] B. Schweer, Phys. Scr. T138 (2009) 014008.
- [12] M. Zlobinski, Fusion Eng. Des. 86 (2011) 1332.
- [13] D. Ivanova, J. Nucl. Mater. 415 (2011) S801.
- [14] V. Phillips, Nucl. Fusion 53 (2013) 093002.
- [15] J.H. Yu, Nucl. Mater. and Energy 12 (2017) 749.
- [16] Th. Loewenhoff, et al., Nucl. Mat. and Energy 9 (2016) 165.
- [17] J.H. Yu, Phys. Scripta T170 (2017) 014009.
- [18] K.A. Walsh, Beryllium chemistry and processing, Mater. Inf. Soc. (2009).
- [19] G.G. Van Eden, Nucl. Fusion 54 (2014) 123010.
- [20] J.H. Yu, Nucl. Fusion 55 (2015) 093027.
- [21] R.P. Doerner, M.J. Baldwin, K. Schmid, Phys. Scr. T111 (2004) 75.
- [22] R.A. Causey, J. Nucl. Mater. 300 (2002) 91.
- [23] G. Longhurst, Tmap7 User Manual, Idaho National Engineering and Environment Laboratory INEEL/EXT-04-02352 (Rev. 2), 2008.
- [24] M. Poon, J. Nucl. Mater. 372 (2008) 390.
- [25] M.J. Baldwin, R.P. Doerner, Nucl. Fusion 57 (2017) 076031.
- [26] W. Eckstein, Calculated Sputtering, Reflection and Range Values, (2002) IPP-report IPP 9/132.
- [27] M.J. Simmonds, J. Nucl. Mater. 508 (2018) 472.
- [28] A. Manhard, J. Nucl. Mater. 415 (2011) S632.
- [29] V.Kh. Alimov, et al., J. Nucl. Mater. 420 (2012) 519.
- [30] L. Gao, Nucl. Fusion 57 (2017) 016026.
- [31] D. Terentyev, Fusion Eng. Des. 124 (2017) 405.
- [32] Ryabtsev, et al., Nuclear Instr. Methods Phys. Res. B 382 (2016) 101–104.
- [33] J. Zhou, H. Tsai, P. Wang, J. Heat Transfer 128 (2005) 680–690.
- [34] J. Roth, K. Schmid, Phys. Scripta T145 (2011) 014031.
- [35] J.H. Yu, Phys. Scr. T159 (2014) 014036.
- [36] M.J. Baldwin, R.P. Doerner, Nucl. Fus. 54 (2014) 083032.
- [37] O.V. Ogorodnikova, J. Appl. Phys. 118 (2015) 074902.
- [38] A. Van Veen, J. Nucl. Mater. 155–157 (1988) 1113.
- [39] W.R. Wampler, J. Nucl. Mater. 122–123 (1984) 1598.